28th Symposium on Naval Hydrodynamics
Pasadena, California, 12-17 September 2010

Multiscale Simulation of Wind–Wave–Structure Interaction

Shengbai Xie, Yi Liu, Di Yang, Xin Guo, and Lian Shen*
(Department of Civil Engineering, The Johns Hopkins University, USA)

Abstract

A multiscale, hybrid simulation capability for the study of wind–wave–structure interaction for naval applications is developed. The simulation consists of a large-scale simulation for wind–wave interaction and a local-scale simulation for air–water–structure interaction. For the oceanic environment, wind and waves are simulated respectively by large-eddy simulation (LES) and high-order spectral (HOS) methods with dynamical interactions between the two. The large-scale and yet wave–phase–resolved wind and wave fields are then used to provide physical inflow condition for the simulation of wind and wave around the structure at the local scale. Around a surface piercing object, a coupled level-set and volume of fluid (CLSVOF) method is used to simulate the air–water coupled flow and the complex interfacial motions. An immersed boundary method (IBM) is coupled with the CLSVOF to simulate the interaction of the object with the surrounding air and water motions. Our simulation result shows that both the wind load and wave load on the object vary with the wave phase and depend on the sea state, indicating the necessity of using the phase-resolved wavefield and its coupled wind turbulence field as the environmental input. The multiscale simulation approach developed in this study may lead to an improved, physics-based, high-resolution prediction tool for wind–wave–structure interaction for naval applications.

1. INTRODUCTION

The problem of wind–wave–structure interaction plays an important role in many naval applications. The sea and wind loads on naval ships directly affect their maneuverability. Under severe sea conditions, forcing from high winds and large-amplitude waves may damage ships and offshore structures. The environmental wind turbulence and the turbulent wake of ship superstructures can also influence the launch and landing of naval aircrafts and ship cargo transfer. Therefore, there is a critical need for the understanding and modeling of wind-waves, the lower part of marine atmospheric boundary layer at various sea states, and wind load and wave load on structures.

The interaction among wind, wave, and structure involves processes of wind and wave evolution at large scales and flow–structure interaction at local scales. Due to the complexity of the problem, existing studies usually have to rely on substantial simplifications. For example, the wave–structure and wind–structure interactions are often treated separately, the results of which are then superimposed to provide a total estimation. In the real marine environment, however, the wind and wave fields are strongly coupled with each other.

Moreover, simplified inflow conditions, such as prescribed waves based on simple wave theories and prescribed mean wind profiles, are often used in the study of flow–structure interaction. These inflow representations can only capture some of the mean flow effect, but miss the irregularity and nonlinearity in the wave field and the turbulence fluctuations in the wind field, which play an essential role in the dynamic response of the structure. The local wind field near the sea surface is highly dependent on the instantaneous wave phase, thus the wind load is also wave coherent.

In this paper, a coupled multi-scale modeling approach is developed for the simulation of wind–wave–structure interaction. For the large-scale simulation, the wind and waves are coupled dynamically, while for the local-scale simulation, the data obtained from large-scale simulation is used as the "real" inflow conditions and the wind–

*Email address for correspondence:LianShen@jhu.edu

wave–structure three-way interaction is simulated without decoupling.

The paper is organized as follows. The numerical methods are introduced in section 2. Two sets of results with different inflow conditions, namely monochromatic wave inflow and broadband irregular wave inflow, are discussed in detail in section 3. Finally, the conclusions are given in section 4.

2. NUMERICAL METHOD

In this study, we develop a multiscale, multiphase, hybrid simulation capability aiming at providing accurate prediction of wind and sea loads on surface piercing objects in realistic oceanic environments. Major developments include: first, coupled LES–HOS simulation at large scales that can capture the dynamical evolution of ocean wavefield under wind action and the details of wind turbulence in the lower part of marine atmospheric boundary layer with the wave phase resolved; second, coupled CLSVOF–IBM method at local scales that can simulate the multiple interactions among wind, wave, and structure, and thus provides prediction of the wind and wave loads.

As shown on the left part of Fig.1, for the far field, we use a coupled LES–HOS approach for the simulation of turbulent wind over complex wavefield. In our simulation, LES is performed for wind turbulence with the sea surface geometry and motion provided by the wave HOS simulation. The LES uses a hybrid pseudo-spectral and finite-difference method on a boundary-fitted grid that follows the wave surface (Yang & Shen, 2010). For the wavefield, we use the HOS method (Dommermuth & Yue, 1987) to capture all of the dynamically important nonlinear wave interactions. The wind pressure result from the LES is supplied to the HOS simulation to obtain wind-wave growth, which then serves as the dynamically evolving boundary condition for the wind LES. The results from large-scale simulation are then used as inflow conditions for the local-scale simulation of wind–wave–structure interaction.

For the local-scale simulation, we use a CLSVOF method for the air–water coupled two-phase flow as shown on the right part of Fig.1. A level-set function is used to represent the air–water interface implicitly (Sussman *et al*, 1994, Osher & Fedkiw, 2001, Sethian & Smereka, 2001). A ghost fluid method is used to capture the interface sharply (Kang *et al*, 2000). A volume of fluid method is coupled with the level-set method to improve the mass conservation (Sussman & Puckett, 2000).

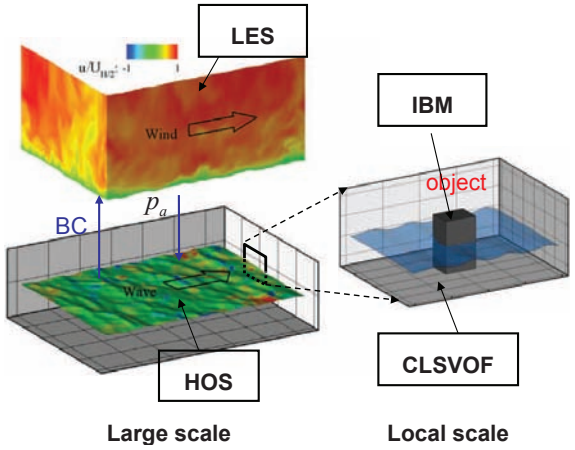

Figure 1: Strategy of large-scale and local-scale simulations.

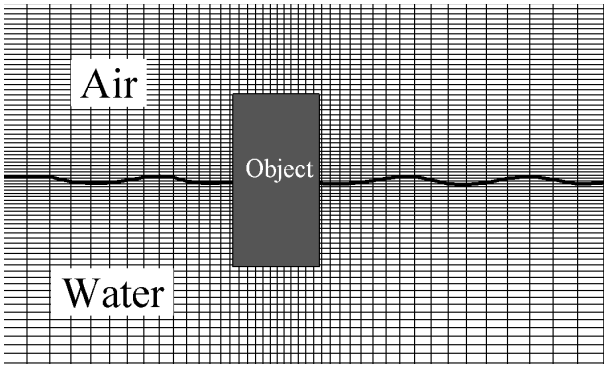

Figure 2: Stretched Cartesian grid on the central vertical plane used in the simulation.

To address the fluid–structure interaction, we use an immersed boundary method (Peskin, 1977, Balaras, 2004, Mittal & Iaccarino, 2005). Spatial discretization is performed on a stretched Cartesian grid as shown in Fig.2. For the CLSVOF–IBM simulation, instantaneous output from the LES–HOS simulation is used as the inflow conditions for the wind and waves. More details of our numerical methods are introduced in the following sections.

2.1. Immersed boundary method

For briefness, we use one-phase flow here to demonstrate the immersed boundary method used in our study. The extension to multiphase flow is straightforward. The governing equations are the unsteady incompressible Navier–

Stokes equations

$$\frac{\partial \mathbf{u}}{\partial t} = -\mathbf{u}\cdot\nabla\mathbf{u} - \frac{1}{\rho}\nabla p + \frac{\mu}{\rho}\nabla^2\mathbf{u} \tag{1}$$

and

$$\nabla\cdot\mathbf{u} = 0 \tag{2}$$

inside the flow domain Ω_f with the boundary condition

$$\mathbf{u} = \mathbf{u}_{\Gamma_b} \tag{3}$$

on the surface Γ_b of the object. Here $\mathbf{u}$ is the velocity vector; p is the pressure; ρ is the density; and μ is the dynamic viscosity. In the immersed boundary method (Balaras, 2004), the boundary condition Eq.3 is combined with the momentum equation Eq.1 in the form of a forcing term, and Eq.1 becomes

$$\frac{\partial \mathbf{u}}{\partial t} = -\mathbf{u}\cdot\nabla\mathbf{u} - \frac{1}{\rho}\nabla p + \frac{\mu}{\rho}\nabla^2\mathbf{u} + \mathbf{f}_b \tag{4}$$

We use the direct discrete forcing approach (Fadlun *et al*, 2000, Mittal & Iaccarino, 2005) to calculate the boundary forcing term $\mathbf{f}_b$ in the above equation. In this approach, first, the right-hand-side terms of Eq.1 are calculated to update the velocity explicitly to obtain $\mathbf{u}^*$

$$\frac{\mathbf{u}^* - \mathbf{u}^n}{\triangle t} = RHS^n = -(\mathbf{u}\cdot\nabla\mathbf{u} + \frac{1}{\rho}\nabla p - \frac{\mu}{\rho}\nabla^2\mathbf{u})^n \tag{5}$$

where n denotes the time step. Next, on the forcing points outside of the body surface (Fig.3), velocity interpolation is performed by a linear tetrahedron-based scheme. The strategy of this step is demonstrated in Fig.3 using a 2D example. The extension from 2D to 3D is straightforward. Denote the interpolated velocity as $\mathbf{u}^{**}$, the forcing term in Eq.4 is then calculated as

$$\mathbf{f}_b^{n+1} = \frac{\mathbf{u}^{**} - \mathbf{u}^*}{\triangle t} \tag{6}$$

The constraint of incompressibility is satisfied by a projection method (Kim & Moin, 1985, Gresho, 1991). The intermediate velocity $\mathbf{u}^*$ is projected into a divergencefree space by solving a Poisson equation:

$$\nabla^2\delta p = \frac{\nabla\mathbf{u}^*}{\triangle t} \tag{7}$$

Finally, the pressure and velocity are updated:

$$p^{n+1} = p^n + \delta p, \qquad \mathbf{u}^{n+1} = \mathbf{u}^* + \triangle t\nabla\delta p \tag{8}$$

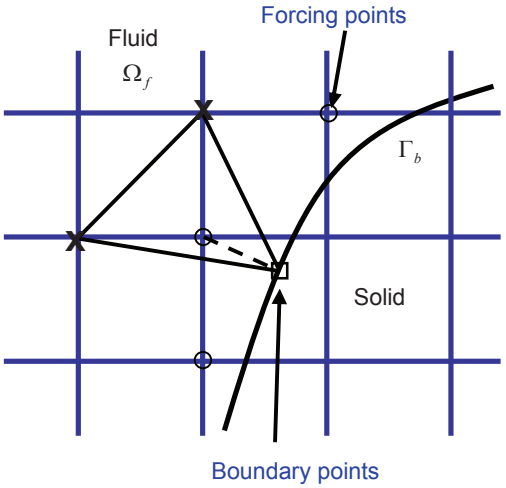

Figure 3: Schematics for the interpolation of velocity to calculate the forcing term. Here ∘ denotes the grid points where the forcing term is applied; □ denotes the points on the body surface used for velocity interpolation; **X** denotes the points in the flow field used for velocity interpolation.

2.2. CLSVOF method

For the two-phase flow of wind and wave, the level-set method (Sussman *et al*, 1994, Osher & Fedkiw, 2001, Sethian & Smereka, 2003) is used, which captures the moving interface implicitly through a signed distance function ϕ defined as

$$\phi(\mathbf{x}) = \begin{cases} d & \text{water} \\ 0 & \text{interface} \\ -d & \text{air} \end{cases} \tag{9}$$

where d is the distance from a point $\mathbf{x}$ to the interface. In Fig.4, the illustration of the distance function (level-set function) ϕ is plotted. The function ϕ is governed by the advection equation

$$\frac{\partial\phi}{\partial t} + \mathbf{u}\cdot\nabla\phi = 0. \tag{10}$$

A reinitialization procedure is used as follows

$$\frac{\partial\phi_c}{\partial\tau} + sign(\phi)(|\nabla\phi_c| - 1) = 0 \tag{11}$$

to conserve the signed distance property as time evolves (Sussman *et al*, 1998). Here τ is artificial time. Using ϕ, the surface normal vector and the curvature are calculated as

$$\mathbf{n} = \frac{\nabla\phi}{|\nabla\phi|} \tag{12}$$

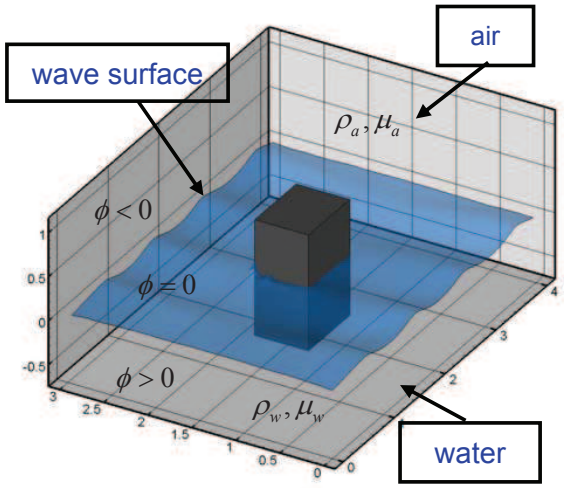

Figure 4: Illustration of level-set function ϕ.

and

$$\kappa = \nabla \cdot \mathbf{n} = \nabla \cdot \frac{\nabla \phi}{|\nabla \phi|}. \tag{13}$$

The non-dimensionalized incompressible Navier–Stokes equations for both the air and the water can be written as one equation

$$\frac{\partial \mathbf{u}}{\partial t} + \nabla \cdot (\mathbf{u}\mathbf{u}) = -\frac{1}{\rho(\phi)} \nabla p + \frac{1}{\rho(\phi) Re} \nabla \cdot (2\mu(\phi)\mathbf{D}) + \frac{\mathbf{k}}{Fr^2} + \frac{1}{\rho(\phi) We} \kappa \delta(\phi) \nabla \phi. \tag{14}$$

with

$$\begin{aligned} \rho(\phi) &= \rho_a H(\phi) + \rho_w (1 - H(\phi)), \\ \mu(\phi) &= \mu_a H(\phi) + \mu_w (1 - H(\phi)). \end{aligned} \tag{15}$$

Here $H(\phi)$ is the Heaviside step function; ρ_a and μ_a are the density and dynamic viscosity of air; ρ_w and μ_w are the density and dynamic viscosity of water; $\mathbf{D} = \frac{1}{2}(\nabla \mathbf{u} + \nabla \mathbf{u}^T)$ is the strain rate tensor; $Re = UL/\nu$, $Fr = \sqrt{U^2/gL}$ and $We = \rho U^2 L/\sigma$ are the Reynolds number, Froude number and Weber number, respectively; $\delta(\phi)$ is the Dirac delta function; $\mathbf{k}$ is the unit vector in the gravity direction.

To improve the mass conservation, volume of fluid (VOF) method is coupled with the level-set method. The following VOF equation (Sussman *et al*, 2000)

$$\frac{\partial F}{\partial t} + \vec{u} \cdot \nabla F = 0 \tag{16}$$

is solved. Here F is the volume fraction of water in each computational cell. Piece-wise linear interface construction method is used to reconstruct the interface and solve the above equation (Ridera & Kothe, 1998). Furthermore,

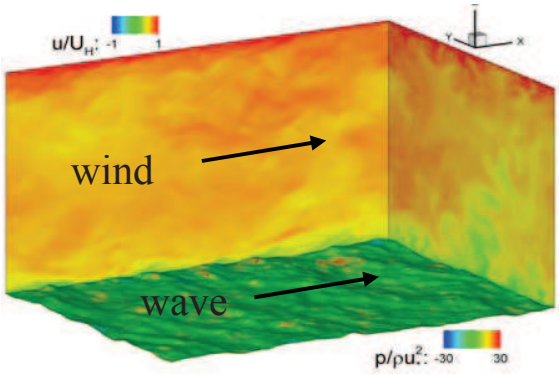

Figure 5: Illustration of coupled wind–wave simulation where streamwise velocity contours are plotted on the vertical planes, and air pressure contours are plotted on the wave surface.

a ghost fluid method is used to treat the air–water interface in a sharp manner (Kang *et al*, 2000). The following interface jump condition

$$\left[\begin{pmatrix} \mathbf{n} \\ \mathbf{T}_1 \\ \mathbf{T}_2 \end{pmatrix} (p\mathbf{I} - \tau)\mathbf{n}^T \right] = \begin{pmatrix} \sigma\kappa \\ 0 \\ 0 \end{pmatrix} \tag{17}$$

is implemented. Here $\mathbf{T}_1$ and $\mathbf{T}_2$ are the two unit tangent vectors; $[\cdot]$ denotes the jump across the interface; and σ is the surface tension. With the ghost fluid method, density and viscosity change sharply across the interface. As a result, the spurious current associated with the smeared interface method is avoided.

3. RESULTS

As a canonical problem, wind blowing over a broadband wavefield that initially satisfies the JONSWAP spectrum is used for the large scale wind–wave simulation. At local scales, a surface piercing hexahedral object inside the wind and wave fields is considered. The object has a forward velocity against the wind and wave direction, i.e., head seas are considered here. We note that while the geometry of the object is simple at the current first step of study, extension to more complex geometries corresponding to naval applications is relatively straightforward with the IBM method used in our study.

For the large-scale LES–HOS coupled simulation, a sub-domain is shown in Fig.5. The wind velocity and pressure distributions are found to be highly dependent on the wave phase (Liu *et al*, 2010). The analysis in their

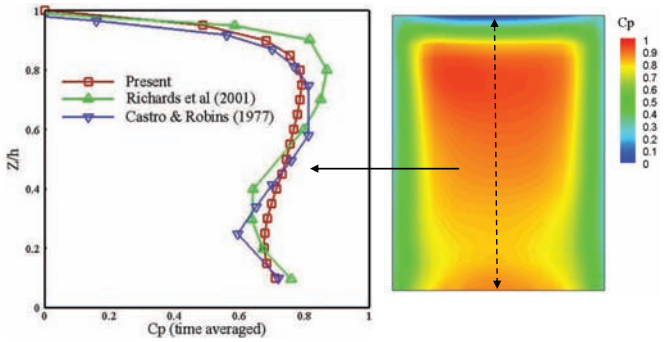

Figure 6: Time-averaged pressure coefficient on the frontal face of the object, and comparison of the center-line profile with the measurements in literature.

paper also shows that the growth rate of each wave component strongly depends on the corresponding wave age, which is defined as the ratio of wave phase speed to the wind friction velocity.

For the local-scale simulation, we first consider the simple case of a monochromatic wave being used as the inflow condition, in order to investigate the dependence of wind load on the wave phase. Next, the broadband wavefield is used as the inflow condition to obtain a more realistic simulation. The details are discussed in the following two subsections.

3.1 Monochromatic wave cases

We simulate an air–water flow passing a hexahedral object with size ratio 1:0.75:2 among the three dimensions. The geometric center of the object is at the mean water surface level. The wave age c/u^* is 2; i.e., the young sea condition is considered here.

In Fig.6, time-averaged value of the pressure coefficient of the wind acting on the frontal face of the object

$$Cp = \frac{P_a}{\frac{1}{2}\rho_a U_h^2} \tag{18}$$

is plotted. Here U_h is the mean value of the streamwise component of velocity at the height of the top of the structure (denoted by the subscript h hereafter). The present result agrees with the experimental data of (Castro & Robins, 1977, Richards *et al*, 2001). The maximum pressure coefficient occurs at about $0.75h$ above the mean water surface, where the wind impinges on the frontal face to form a stagnation point (Peterka *et al*, 1985) as shown in Fig.7. Near this stagnation point, flow goes outward toward the edges of the frontal face. A local minimum

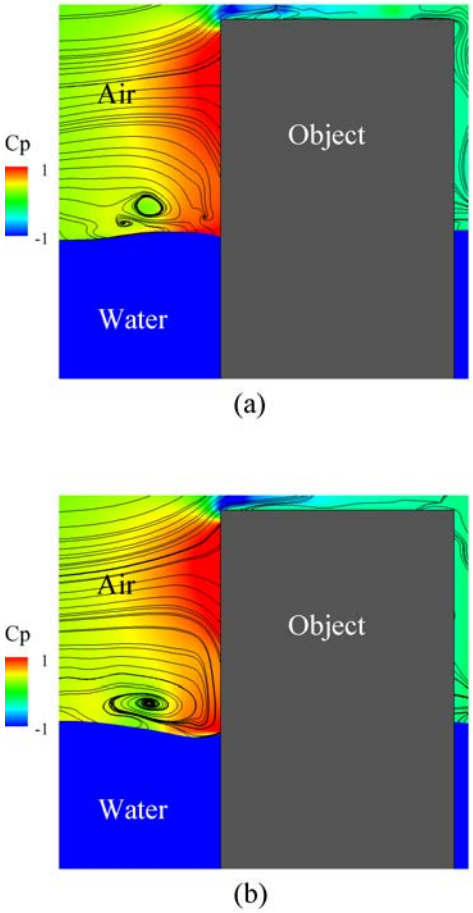

Figure 7: Instantaneous streamline patterns and pressure contours on the center plane cutting through the object when: (a) a crest arrives at the object; (b) a trough arrives at the object.

of pressure coefficient is found at about $0.2h$ above the mean water surface, because there exists a horseshoe vortex (Peterka *et al*, 1985) at that location as plotted in Fig.7. Because of the horseshoe vortex, a bottleneck shape is observed on the pressure contours (Fig.6).

Since the ratio of the object length to the wavelength is 1/1.7 (see Fig.8), the frontal and rear sides of the object are not at the same wave phase. For instance, in Fig.8, when the crest of the wave reaches the frontal face, the rear face is between a crest and a trough. Moreover, the plane progressive wave is distorted around the object, especially behind the object as shown in Fig.8, although the overall geometry of the wave surface still maintains.

In our following analysis of the phase dependence of streamwise wind load, we consider the frontal face only.

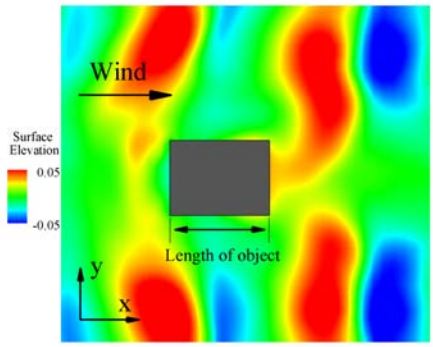

Figure 8: Top view of the surface elevation surrounding the object when a wave crest arrives at the frontal face of the object; and

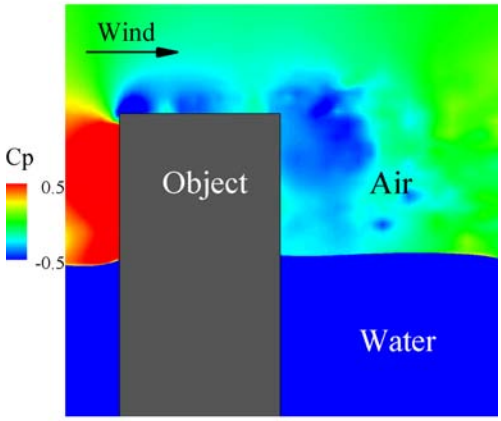

Figure 10: The low pressure wake caused by the flow separation at the object.

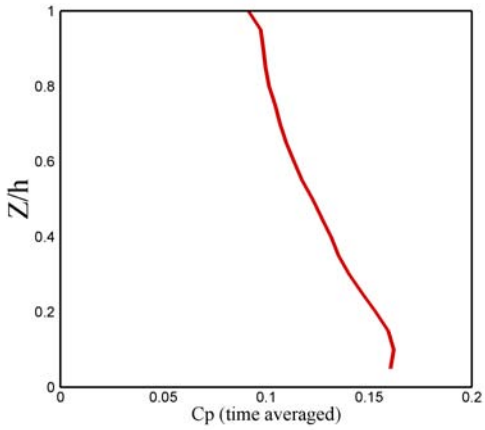

Figure 9: Vertical central section wind pressure coefficients on the rear face.

In Fig.9, the time averaged pressure coefficient profile along the vertical central line on the rear face is plotted. Compared with the result on the frontal face in Fig.6, it is clear that the load on the rear face is much smaller (Richards *et al*, 2001) due to the lower pressure inside the wake region behind the object as shown in Fig.10. We also found that the variation of wind load over the different wave phases is small too (results not shown here due to space limitation). On the other hand, the air pressure acting on the frontal face varies considerably at different wave phases. A typical example is shown in Fig.7. When a crest reaches the frontal face (Fig.7a), the pressure is larger than that when a wave trough arrives (Fig.7b). The oscillation of wind load is mainly caused by the variation of the air pressure acting on the frontal face during the different wave phases.

In order to show the wave-phase dependence of the wind load more clearly, the wave-phase averaged pressure coefficient distribution along the vertical central line on the frontal face is plotted in Fig.11. It confirms that the pressure at crest is higher than that at trough. The maximum of the difference occurs near the air–water interface. As the height increases, the difference reduces gradually. Above $z = 0.6h$, the difference is negligible.

The wave-phase dependence of the wind load is caused by the periodic variation of the wind speed above the wave surface. It is found that above the wave crest, the wind speed is larger and the shear in the air flow is stronger compared with those above the wave trough. The difference of the velocity gradient at these two wave phases is demonstrated in Fig.12. As the height increases, the influence of the wave phase on the wind speed is reduced. Fig.11 shows that near the stagnation point, the pressure distributions are quite similar between the wave crest phase and the trough phase. As a result, the wind load on the upper part of the object is less affected by the wave passage.

Moreover, the existence of the horseshoe vortex at the frontal corner also influences the wind load on the frontal face since it forms a low-pressure region. The position of the vortex oscillates with time, as shown in Fig.7. The center of the vortex moves mainly along the streamwise and vertical directions at different wave phases.

We next study the relation between the angle of attack and the wind load. Three angles are discussed in this paper, $\varepsilon = 0^\circ$, 30° and 60°. Following Blendermann (1994), we decompose the force along different directions as shown in Fig.13. Accordingly, the drag coefficient *CD*

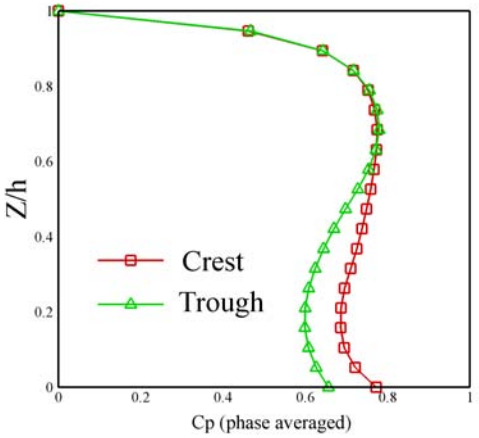

Figure 11: Profiles of wave-phase averaged pressure coefficient along the vertical central line on the frontal face of the object for wave crest and wave trough.

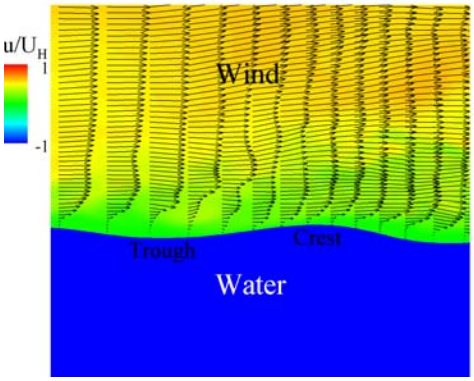

Figure 12: Instantaneous velocity vectors above the wave surface.

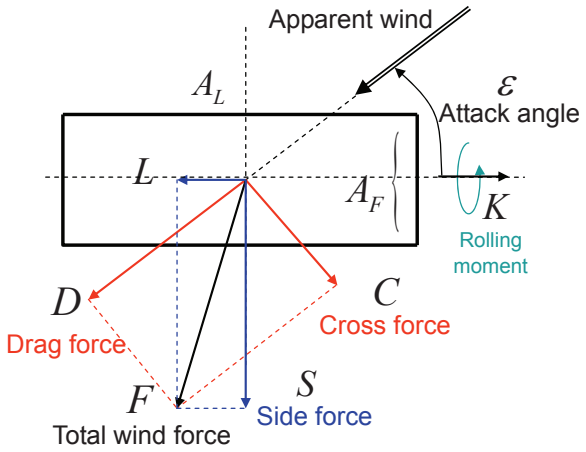

Figure 13: Definition of wind forces and moments.

and the cross force coefficient CL are defined as

$$CD = \frac{D}{\frac{1}{2}\rho_a U_h^2 A_L} \tag{19}$$

$$CC = \frac{C}{\frac{1}{2}\rho_a U_h^2 A_L} \tag{20}$$

where D and C are the drag and cross forces defined in Fig.13, and A_L is the mean lateral area of the object above the water. The longitudinal force coefficient CL and the side force coefficients CS are

$$CL = \frac{L}{\frac{1}{2}\rho_a U_h^2 A_L} \tag{21}$$

$$CS = \frac{S}{\frac{1}{2}\rho_a U_h^2 A_L} \tag{22}$$

where L and S are the longitudinal force and the side force defined in Fig.13, respectively. The rolling moment coefficient CK is defined as

$$CK = \frac{K}{\frac{1}{2}\rho_a U_h^2 A_L h} \tag{23}$$

where K is the rolling moment.

Table 1 and 2 show the force coefficients for different angles of attack conditioned upon the wave crest and wave trough phases. From Table 1, there are several observations. First, both the longitudinal force coefficient CL and the drag coefficient CD are wave-phase dependent. When a wave crest arrives at the frontal face of the object, wind force is stronger than that when a wave trough arrives. This result is consistent with our previous finding for the $\varepsilon = 0^\circ$ case.

Second, the drag coefficient CD increases with the angle of attack. This is partially due to the increase of projected area. Also, the separation of the flow behind the

	ε	Trough	Crest	Increase
CL	0°	0.403	0.555	37.9%
	30°	0.555	0.605	9.1%
	60°	0.409	0.510	24.7%
CD	0°	0.403	0.555	37.9%
	30°	0.748	0.788	5.4%
	60°	0.900	0.938	4.2%

Table 1: Longitudinal and drag force coefficients.

	ε	Trough	Crest	Increase
CS	0°	0.0522	0.0521	−0.2%
	30°	0.533	0.528	−0.9%
	60°	0.805	0.790	−1.8%
CC	0°	0.0522	0.0521	−0.2%
	30°	0.183	0.155	−15.1%
	60°	0.049	-0.047	−4.1%

Table 2: Side and cross force coefficients.

object becomes stronger as the attack angle increases, to form a larger region of low pressure behind the object as shown in Fig.14. In the figure, the increase of turbulence intensity in the wake region with the angle of attack is also noticeable.

Third, the longitudinal force coefficient *CL* at $\varepsilon = 30^\circ$ is larger than that at 0° and 60°. The flow separation behind the object is stronger at 30° than that at 0° as plotted in Fig.14(a) and Fig.14(b), which leads to lower pressure on the rear face at 30°. The flow separation at 60° is also strong, but the maximum of pressure is not on the frontal face but on a side face instead, as shown in Fig.14(c), which makes its longitudinal pressure difference less than that at 30°. From Table 2, it is also found that the side force coefficient *CS* increases with the angle of attack, and is not sensitive to the wave phase. The cross force coefficient *CC* is the largest at the attack angle 30°, which has the largest asymmetry of wind load among the three cases as shown in Fig.14.

The rolling moment coefficient *CK* is plotted in Fig.15 as a function of the angle of attack. The total rolling moment is decomposed into wind and water parts. The sign of the coefficient indicates the rolling direction. In the present study, the pivot axis is on the air–water interface along the longitudinal direction of the object. From Fig.16, we can see the tendency that the magnitude of *CK* increases with the angle of attack. This is as expected because the rolling moment is closely related to the side force coefficient *CS* that also increases monotonically with the angle of attack as shown earlier.

Another interesting observation from Fig.15 is that the wind-induced rolling moment dominates the wave-induced moment for the wind and wave conditions considered in the present simulation. In other words, for a slow wave with strong wind, the rolling effect of the wind load is important to the safety of vessels or offshore structures.

Finally, the drag coefficient of the wave CD_w

$$CD_w = \frac{D_w}{\frac{1}{2}\rho_w U_p^2 A_L} \tag{24}$$

in a wave period is plotted in Fig.17. Here, D_w is the drag force of water, and U_p is the phase speed of the wave. As shown in Fig.17, CD_w is strongly dependent on the wave phase. Because the wave speed is slow in this case, the variation of hydrostatic pressure associated with the surface elevation plays an important role in the wave drag.

3.2 Broadband wave cases

In this subsection we consider more complex and realistic situations in which inflow condition from a large-scale simulation of a broadband wavefield with the JONSWAP spectrum is used for the local-scale wind–wave–structure simulation. As expected, the wave and wind fields are more complex than the monochromatic wave case. Nevertheless, the salient features of the flow field and wind load remain the same. In Fig.18, the wind pressure coefficient along the vertical central section is plotted. Similar to the monochromatic wave case, a horseshoe vortex is generated near the lower corner of frontal face (Fig.20), resulting in a local minimum of pressure near the wave surface, which corresponds to the local minimum near Position 0 in Fig.18. Note that the size of the horseshoe vortex is bigger in the case here (Fig.20) than in the monochromatic-wave case (Fig.15). This is due to the thicker boundary layer of the inflow here as shown in Fig.21. Similar effect of boundary layer thickness on the horseshoe was discussed by Baetke *et al* (1990). The wind flow separates at the leading edge (Position 1 in Fig.18), which causes a pressure minimum there. Vortex shedding happens on the roof (Fig.20), corresponding to Positions 1 to 2 in Fig.18. The pressure variation near the leading edge is significant. It is also found that the separation on the roof is stronger in this case than that in the monochromatic wave case as shown in Fig.21. The separation of the flow from the object makes the pressure on the rear face (Position 2 to 3 in Fig.18) much lower than the pressure on the frontal face but relatively higher than that on the roof. Moreover, as shown in Fig.19, low pressure regions are formed on both side faces, also due to flow separation.

In Fig.22, the flow separation process on the roof and rear of the object on the central vertical plane is plotted.

The wave behind the object becomes flatter. As a result, the wind wake behind the object is less influenced by the wave phase. In some sense the flow pattern behind the object resembles more what is in the flat ground cases (Hunt *et al*, 1978, Baetke *et al*, 1990). At some distance downstream, the separated flow reattaches to the wave surface.

In Fig.23, the wind pressure distributions on the frontal face of the object are plotted for two different wave phases. The pressure is higher when a local crest arrives at the frontal face than that when a local trough arrives. This phenomenon is similar to that in the monochromatic wave case, in that the wind load is wave-phase dependent. Since the wave condition is much more complex in this case, the wave-phase dependence may be affected not only by the local wave phase, but also by a combination of different waves. The latter needs further investigation.

The instantaneous flow fields at angles of attack of $\varepsilon = 30^\circ$ and 60° are plotted in Fig.24. Compared with Fig.20, it is shown that the turbulence intensity behind the object increases with the angle, in a way similar to what is shown in the monochromatic-wave case (Fig.15). Note that the turbulence intensity above the wave surface in the broadband wave case is higher, because the geometry of the wave surface is much more complex.

4. CONCLUSIONS

In this study, we develop a multiscale, hybrid simulation capability for wind–wave–structure interaction. The coupled CLSVOF–IBM provides an accurate and robust tool for the study of air and water free-surface flows around a structure. To represent the oceanic environment faithfully, a coupled LES–HOS method is developed to simulate large-scale wind and wave fields, from which realistic inflow condition is obtained for the CLSVOF–IBM simulation. Our simulation result shows salient wave-coherent flow structure in the wind field. We also elucidate the inherent relationship between the wave dynamics and the wind and wave loads on surface piercing structures using a monochromatic wave case. For the more complex and realistic broadband wave cases, the characteristic features of the monochromatic wave case still obtain, but in a more complex form as expected. This study suggests that incorporating the multiscale wind–wave–structure interaction dynamics may be helpful for the design and operation of naval ships in complex marine environments under various sea conditions.

References

[1] F. Baetke, H. Werner, and H. Wengle, *Numerical simulation of turbulent flow over surface-mounted obstacles with sharp edges and corners.*, Journal of Wind Engineering and Industrial Aerodynamics **35** (1990), 129–147.

[2] E. Balaras, *Modeling complex boundaries using an external force field on fixed cartesian grids in large-eddy simulations.*, Computers & Fluids **33** (2004), 375–404.

[3] W. Blendermann, *Parameter identification of wind loads on ships*, Journal of Wind Engineering and Industrial Aerodynamics **51** (1994), 339–351.

[4] I.P. Castro and A.G. Robins, *The flow around a surface-mounted cube in uniform, turbulent streams.*, Journal of Fluid Mechanics **79** (1977), 307–335.

[5] D.G. Dommermuth and D.K.P. Yue, *A high-order spectral method for the study of nonlinear gravity waves.*, Journal of Fluid Mechanics **184** (1987), 267–288.

[6] E.A. Fadlun, R. Verzicco, P. Orlandi, and Mohd-Yusof, *Combined immersed boundary finite-difference methods for three-dimensional complex flow simulation.*, Journal of Computational Physics **165** (2000), 35–66.

[7] P.M. Gresho, *Incompressible fluid dynamics: some fundamental formulation issues.*, Annual Review of Fluid Mechanics **23** (1991), 413–453.

[8] J.C.R. Hunt, C.J. Abell, J.A. Peterka, and H. Woo, *Kinematical studies of the flows around free or surface-mounted obstacles; applying topology to flow visualization.*, Journal of Fluid Mechanics **86** (1978), 179–200.

[9] M. Kang, R.P. Fedkiw, and X. Liu, *A boundary condition capturing method for multiphase incompressible flow.*, Journal of Scientific Computing **15** (2000), no. 3, 323–360.

[10] J. Kim and P. Moin, *Application of a fractional-step method to incompressible navier-stokes equations.*, Journal of Computational Physics **59** (1985), 308–323.

[11] X. Liu, R.P. Fedkiw, and M. Kang, *A boundary condition capturing method for*

poisson's equation on irregular domain., Journal of Computational Physics **160** (2000), 151–178.

[12] Y. Liu, D. Yang, X. Guo, and L. Shen, *Numerical study of pressure forcing of wind on dynamically evolving water waves.*, Physics of Fluids **22** (2010), 041704.

[13] R. Mittal and G. Iaccarino, *Immersed boundary method.*, Annual Review of Fluid Mechanics **37** (2005), 239–261.

[14] S. Osher and R. Fedkiw, *Level set methods: an overview and some recent results 1.*, Journal of Computational Physics **169** (2001), 463–502.

[15] C.S. Peskin, *Numerical analysis of blood flow in the heart.*, Journal of Computational Physics **25** (1977), 220–252.

[16] J.A. Peterka, R.N. Meroney, and K.M. Kothari, *Wind flow patterns about buildings.*, Journal of Wind Engineering and Industrial Aerodynamics **21** (1985), 21–38.

[17] P.J. Richards, R.P. Hoxey, and L.J. Short, *Wind pressures on a 6m cube.*, Journal of Wind Engineering and Industrial Aerodynamics **89** (2001), 1553–1564.

[18] W.J. Ridera and D.B. Kothe, *Reconstructing volume tracking.*, Journal of Computational Physics **141** (1998), 112–152.

[19] J.A. Sethian and P. Smereka, *Level set methods for fluid interfaces.*, Annual Review of Fluid Mechanics **35** (2003), 341–372.

[20] M. Sussman, E. Fatemi, P. Smereka, and S. Osher, *An improved level set method for incompressible two-phase flows.*, Computers & Fluids **27** (1998), no. 5-6, 663–680.

[21] M. Sussman and E.G. Puckett, *A coupled level set and volume-of-fluid method for computing 3d and axisymmetric incompressible two-phase flows.*, Journal of Computational Physics **162** (2000), 301–337.

[22] M. Sussman, P. Smereka, and S. Osher, *A level set approach for computing solutions to incompressible two-phase flow.*, Journal of Computational Physics **114** (1994), 146–159.

[23] D. Yang and L. Shen, *Direct simulation based study of turbulent flow over various waving boundaries.*, Journal of Fluid Mechanics **650** (2010), 131–180.

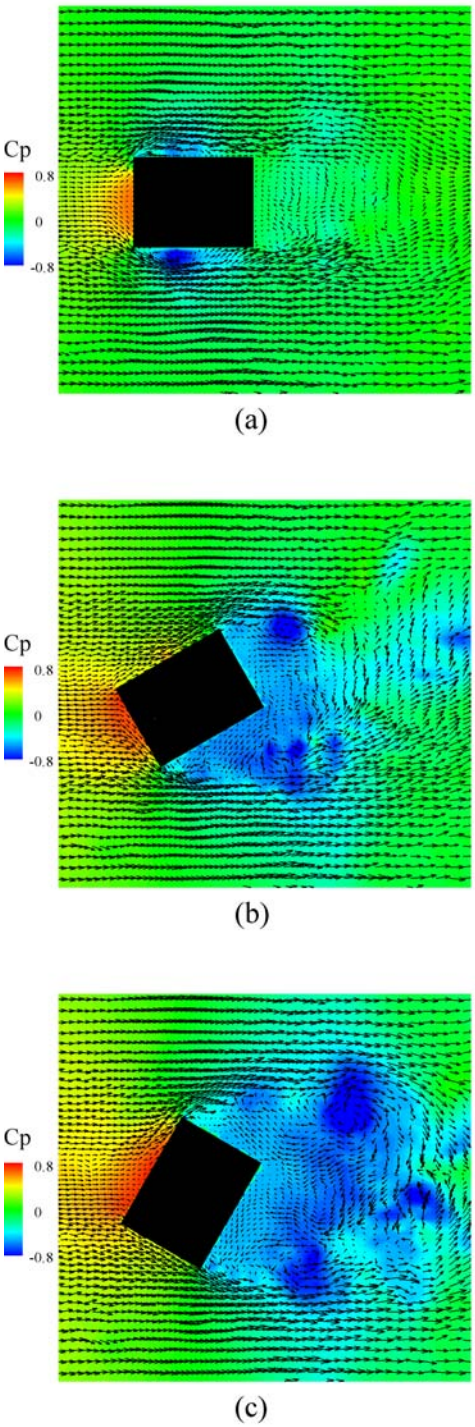

Figure 14: Top view of instantaneous distribution of pressure contours and velocity vectors at a height of $z = 0.5h$ for angle of attack of: (a) $\varepsilon = 0^\circ$; (b) $\varepsilon = 30^\circ$; (c) $\varepsilon = 60^\circ$

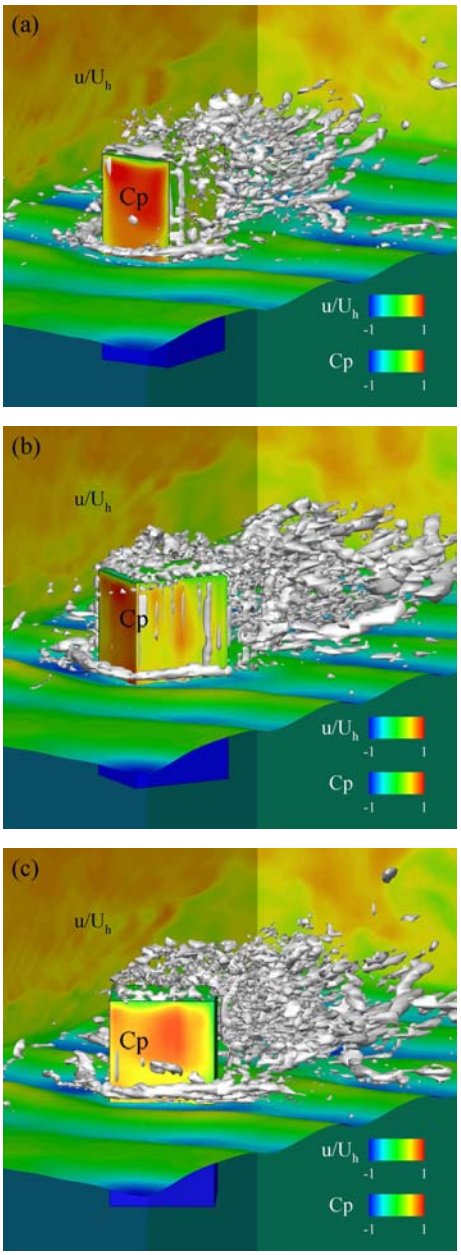

Figure 15: Coherent vortical structures in the wind around the object for angle of attack of: (a) $\varepsilon = 0^\circ$; (b) $\varepsilon = 30^\circ$; (c) $\varepsilon = 60^\circ$.

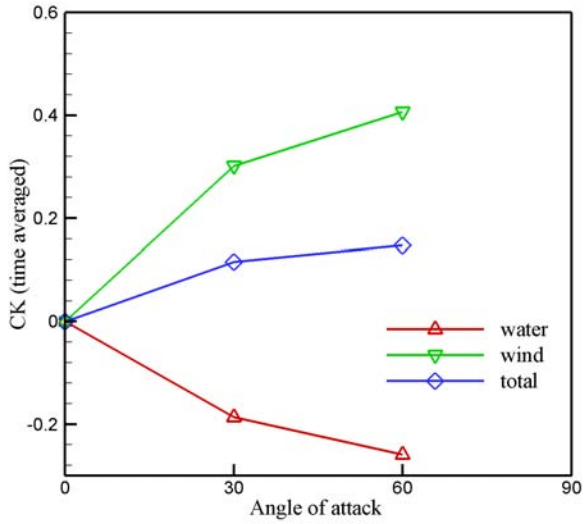

Figure 16: Rolling moment coefficient at different angles of attack.

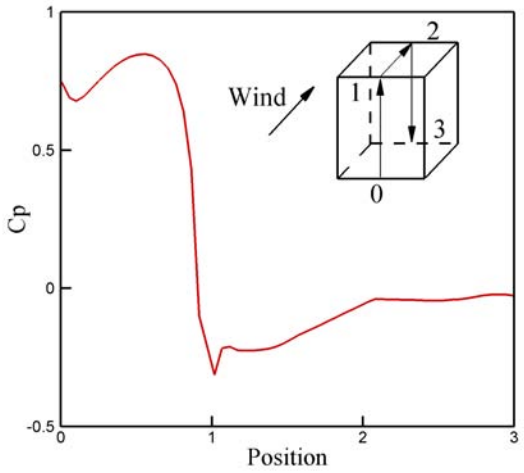

Figure 18: Profile of time-averaged wind pressure coefficient along the vertical mid-section of the object.

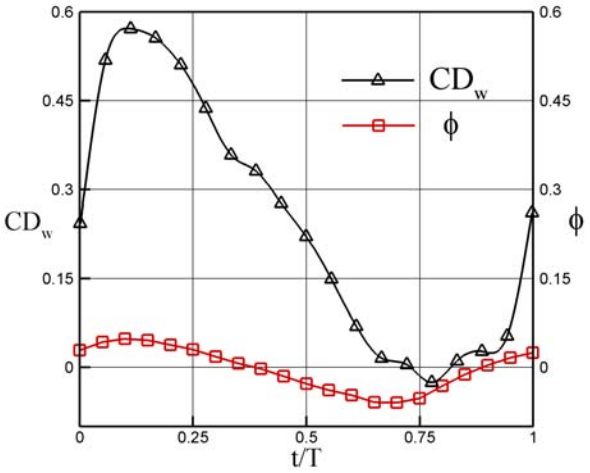

Figure 17: Variation of drag coefficient on the waterside over one wave period. Here ϕ indicates the wave surface elevation.

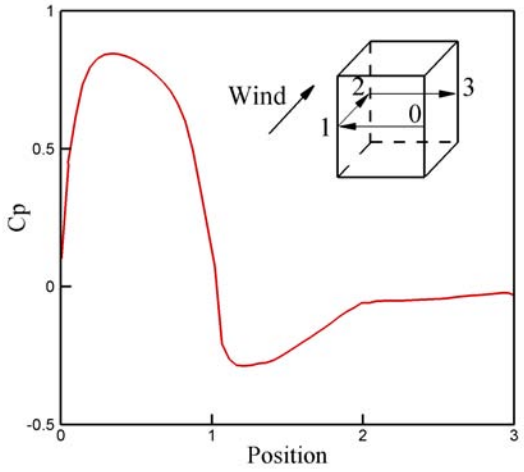

Figure 19: Profile of time-averaged pressure coefficient along the horizontal section at the mid height of the object.

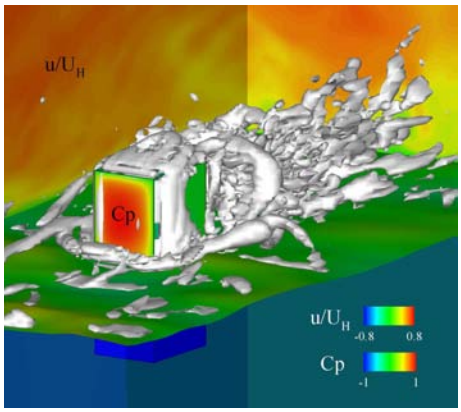

Figure 20: Coherent vortical structures in the wind around the object for angle of attack of $\varepsilon = 0°$.

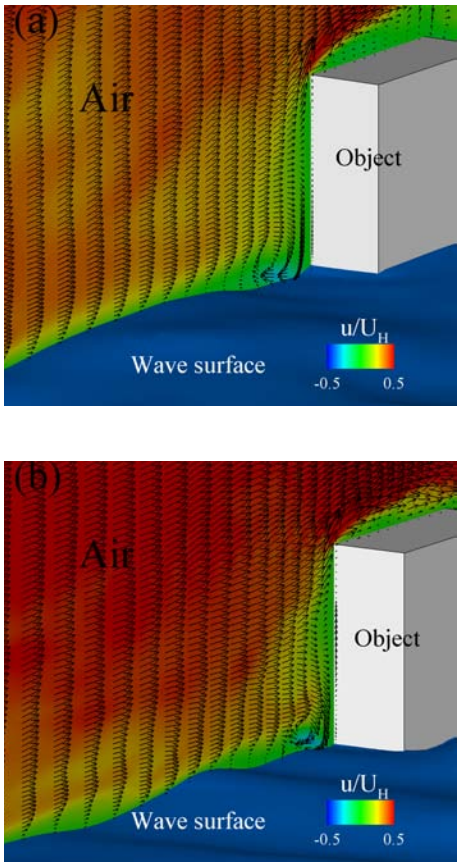

Figure 21: Instantaneous velocity vectors in the vertical central plane above the wave surface for: (a) broadband wave case; (b) monochromatic wave case.

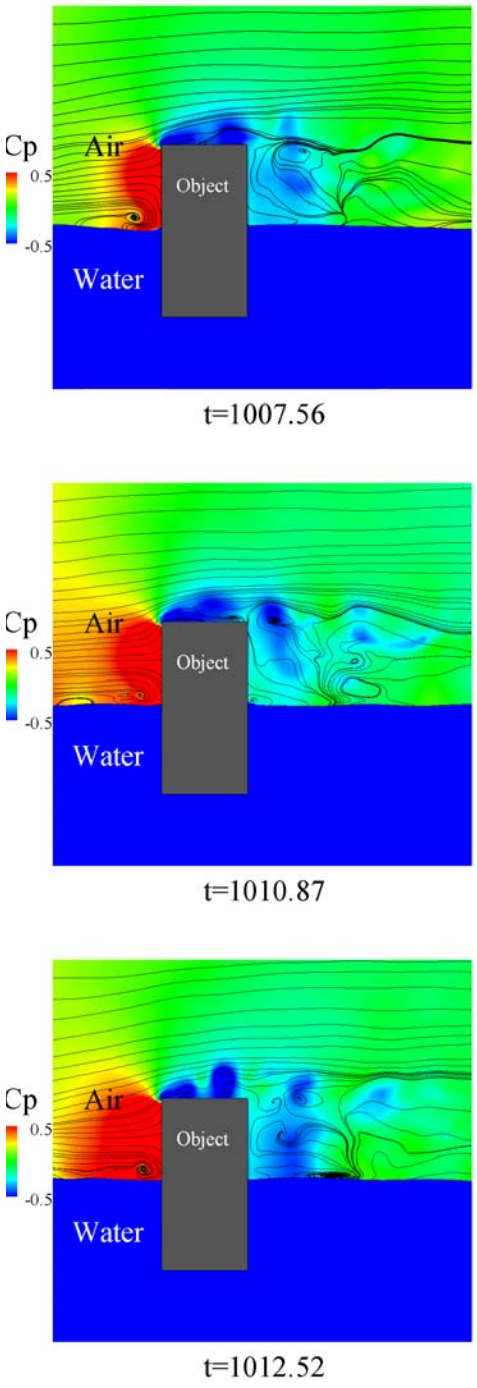

Figure 22: Time evolution of flow field around the object on the vertical central plane at three instants. Plotted are pressure coefficient contours and streamlines.

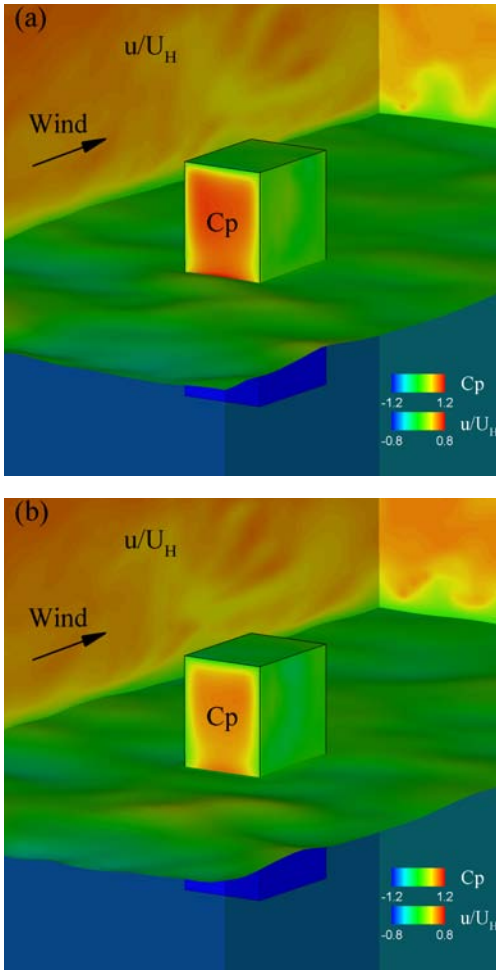

Figure 23: Wind pressure distribution on the frontal face at different wave phases: (a) a local crest reaches the object; (b) a local trough reaches the object.

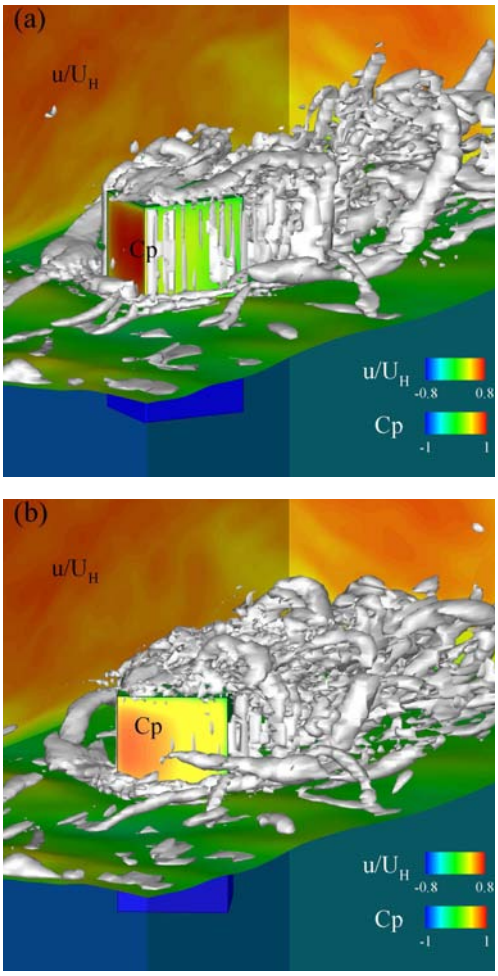

Figure 24: Coherent vortical structures in the wind around the object for angle of attack of: (a) $\varepsilon = 30^{\circ}$; (b) $\varepsilon = 60^{\circ}$.